Semiconductor Science and Technology

Electron transport lifetimes in InSb/Al_{1-x} In_x Sb quantum well 2DEGs

OPEN ACCESS
IOP Publishing
Semiconductor Science and Technology
Semicond. Sci. Technol. **32** (2017) 085002 (8pp)
https://doi.org/10.1088/1361-6641/aa75c8

Electron transport lifetimes in $InSb/Al_{1-x}In_xSb$ quantum well 2DEGs

D G Hayes[1], C P Allford[1], G V Smith[1,4], C McIndo[1], L A Hanks[1,5], A M Gilbertson[2], L F Cohen[2], S Zhang[3], E M Clarke[3] and P D Buckle[1]

[1] School of Physics and Astronomy, Cardiff University, Queen's Buildings, The Parade, Cardiff, CF24 3AA, United Kingdom
[2] Blackett Laboratory, Imperial College London, Prince Consort Road, London, SW7 2BZ, United Kingdom
[3] EPSRC National Centre for III-V Technologies, North Campus, University of Sheffield, Sheffield, S3 7HQ, United Kingdom

E-mail: HayesD3@cardiff.ac.uk

Received 23 February 2017, revised 26 May 2017
Accepted for publication 30 May 2017
Published 4 July 2017

Abstract

We report magnetotransport measurements of $InSb/Al_{1-x}In_xSb$ modulation doped quantum well (QW) structures and the extracted transport (τ_t) and quantum (τ_q) lifetime of carriers at low temperature (<2 K). We consider conventional transport lifetimes over a range of samples with different doping levels and carrier densities, and deduce different transport regimes dependent on QW state filling calculated from self-consistent Schrödinger–Poisson modelling. For samples where only the lowest QW subband is occupied at electron densities of $2.13 \times 10^{11}\,cm^{-2}$ and $2.54 \times 10^{11}\,cm^{-2}$ quantum lifetimes of $\tau_q \approx 0.107$ ps, and $\tau_q \approx 0.103$ ps are extracted from Shubnikov–de Haas oscillations below a magnetic field of 0.8 T. The extracted ratios of transport to quantum lifetimes, $\tau_t/\tau_q \approx 17$ and $\tau_t/\tau_q \approx 20$ are similar to values reported in other binary QW two-dimensional electron gas systems, but are inconsistent with predictions from transport modelling which assumes that remote ionized donors are the dominant scattering mechanism. We find the low τ_t/τ_q ratio and the variation in transport mobility with carrier density cannot be explained by reasonable levels of background impurities or well width fluctuations. Thus, there is at least one additional scattering mechanism unaccounted for, most likely arising from structural defects.

Keywords: indium antimonide, quantum well 2DEG, magnetotransport, quantum lifetime, transport mobility

(Some figures may appear in colour only in the online journal)

1. Introduction

Indium antimonide (InSb) exhibits the lowest reported electron effective mass ($m^* = 0.014\,m_e$) [1] and highest reported room-temperature electron mobility ($\mu_e = 78\,000\,cm^2\,V^{-1}\,s^{-1}$) [1] of any compound semiconductor. These properties make InSb particularly suited to certain electronic applications and has allowed for the development of low voltage millimetre-wave transistors in comparison to more conventional gallium arsenide (GaAs) and indium phosphide (InP) based devices. There has been a recent resurgence of interest in the development of high quality InSb material following the report of two-dimensional electron gas (2DEG) channel mobilities in excess of $200\,000\,cm^2\,V^{-1}\,s^{-1}$ at $T = 1.8$ K [2–4], and the possibility of Majorana Fermion observation in InSb nanowires [5, 6].

[4] Author to whom any correspondence should be addressed.
[5] Present address: Physics Department, Lancaster University, LA1 4YB.

Furthermore, the strong spin–orbit interaction and extremely large Landé g-factor ($g \approx -50$) [1, 7, 8] exhibited in InSb has gained attention for potential exploitation in spintronics and quantum information control [9–11]. In such applications, the transport lifetime (τ_t) and electron quantum lifetime (τ_q), are useful figures of merit, where the latter is a measure of the mean lifetime of electrons in cyclotronic motion between momentum scattering events. There have been numerous studies of both electron transport and electron quantum lifetimes in more conventional III-V semiconductors [12–15]. However, only the electron transport mobility and transport lifetime have been examined previously in InSb quantum well (QW) 2DEGs [4, 16, 17].

In this paper we present magnetotransport measurements of high mobility InSb/$Al_{1-x}In_xSb$ modulation doped QW heterostructures with varying electron mobilities and carrier densities. We extract the electron transport and quantum lifetimes of carriers at low temperature ($\leq$2 K) and examine the extracted ratio of transport to quantum lifetimes, τ_t/τ_q, with comparison to theoretically calculated values from self-consistent Schrödinger–Poisson and transport modelling.

2. Growth and sample details

The InSb QW heterostructures studied were grown by solid source molecular beam epitaxy (MBE) on semi-insulating, lattice mismatched GaAs substrates. In growth order, the epitaxy comprises an aluminium antimonide (AlSb) accommodation layer, a 3 μm $Al_{0.1}In_{0.9}Sb$ strain-relieving barrier layer (to allow for mismatch relaxation), a 30 nm InSb QW layer and a 50 nm $Al_{0.15}In_{0.85}Sb$ top barrier layer. Tellurium (Te) δ-doping is introduced only into the top barrier, 25 nm above the InSb QW. Deliberate doping of the lower barrier is avoided in order to prevent any impurity donor atoms being carried forward on the growth plane which could significantly increase the scattering rate of carriers in the QW. We report on a series of wafers with varying δ-dopant concentrations. Wafers were grown in two growth campaigns, several months apart. Wafers from the same campaign were grown within days of each other, and thus assumed to comprise near identical background impurities.

Hall bar devices with an aspect ratio of 5:1 (nominally 200 μm × 40 μm) were fabricated using standard contact photolithography, mesa wet etching and metal deposition techniques. All fabrication processes were carried out below $T \sim 100$ °C to prevent excess metal penetration and Te dopant migration in the samples. The fabricated devices were mounted into non-magnetic packages and contact between the package and devices made via fine gold wire bonding.

3. Measurement of transport lifetime and quantum lifetime

Hall measurements at magnetic fields up to $B = 0.5$ T were made on each sample between room temperature and $T = 3$ K. To evaluate the InSb 2DEG properties, the aspect ratio of each Hall bar was obtained using a calibrated optical microscope, and used in two-carrier analysis of the data [18]. Figure 1 shows the extracted Hall mobility (μ_{Hall}) and Hall sheet carrier density (n_{Hall}) against temperature of the carrier localised to the InSb QW for sample A. It can be seen that the magnetotransport behaviour below $T \sim 30$ K is temperature independent, whilst the variation of the mobility with temperature is described and modelled for sample A in section 5.

A general trend can be seen in figure 2 between the Hall mobility and Hall sheet carrier density extracted from two-carrier fits at $T < 5$ K for various samples from the two growth campaigns. The earlier campaign (solid square symbols) includes samples A and B which have measured values of $n_{Hall} = 2.14 \times 10^{11}$ cm^{-2}, $\mu_{Hall} = 168\,000$ cm^2 V^{-1} s^{-1} and $n_{Hall} = 2.47 \times 10^{11}$ cm^{-2}, $\mu_{Hall} = 179\,000$ cm^2 V^{-1}s^{-1} respectively. The later growth campaign consists of a series of five samples with increasing δ-doping levels (solid diamond symbols), which include a sample with measured $n_{Hall} = 2.90 \times 10^{11}$ cm^{-2} and $\mu_{Hall} = 242\,000$ cm^2 V^{-1} s^{-1} (sample C). The samples with approximately the same carrier density as those in the first campaign exhibit consistently higher mobility, suggesting that growth quality has improved between the two campaigns. The behaviour of the transport mobility with Hall sheet carrier density is discussed in section 4.

A mean transport lifetime (τ_t) can be derived from the Drude model if it is assumed that $\mu_{Hall} = \mu_{drift}$, using the relation $\tau_t = (\mu_{Hall} m^*)/e$. We note that care must be taken to use the correct effective mass after accounting for strain and non-parabolicity in the InSb QW conduction band. A four band **k.p** model which accounted for the strained InSb QW bandgap and lattice constant, with values taken from [19] was used to calculate effective masses of $m^* = 0.0195\ m_e$ and $m^* = 0.0200\ m_e$ for samples A and B respectively. The transport lifetimes were therefore calculated to be $\tau_t = 1.86$ and $\tau_t = 2.04$ ps.

The quantum lifetime of carriers in a 2DEG can be extracted by analysis of the amplitude of the observed oscillation in the longitudinal resistance at low magnetic field (Shubnikov-de Haas, SdH oscillation), where the peak values, $\Delta R_{xx}(B)$, are given by [20],

$$\Delta R_{xx}(B) = R_0 4 D_T(X_T)\ \exp(-D_q/\hbar\omega_c), \tag{1}$$

where only the first harmonic of the Fourier expansion is retained. In equation (1), R_0 is the zero field resistance, $D_q\left(=\frac{\hbar\pi}{\tau_q}\right)$ is the Dingle damping term [21], and $D_T(X_T)$, is the thermal damping term given by,

$$D_T(X_T) = \frac{X_T}{\sinh(X_T)}, \tag{2}$$

where X_T is given by,

$$X_T = \frac{2\pi^2 k_B T}{\hbar\omega_c} \tag{3}$$

and where k_B is the Boltzmann constant and $\hbar\omega_c$ is the cyclotron energy. It is trivial to see that a semi-log plot of D_P against $1/B$ (a so called 'Dingle plot') yields the quantum

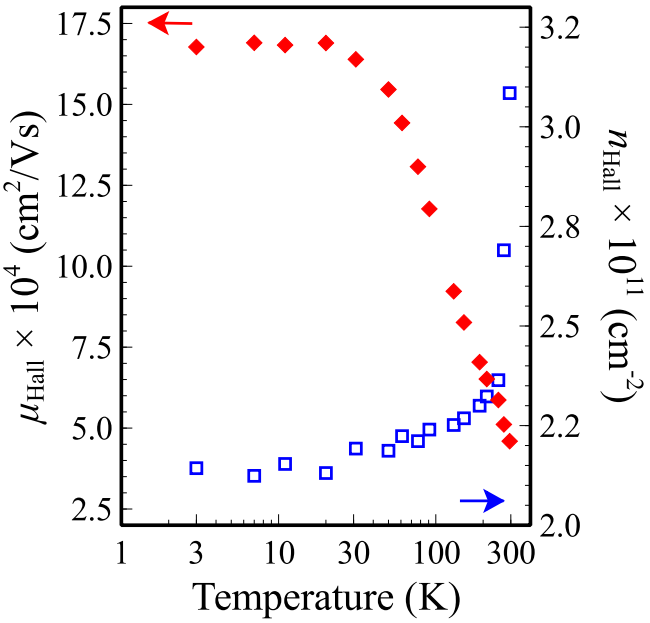

Figure 1. Measured Hall mobility (μ_{Hall}, solid diamonds) and Hall sheet carrier density (n_{Hall}, hollow squares) against temperature for the carrier localised to the InSb quantum well from two-carrier analysis of Hall measurements up to $B = 0.5$ T for sample A.

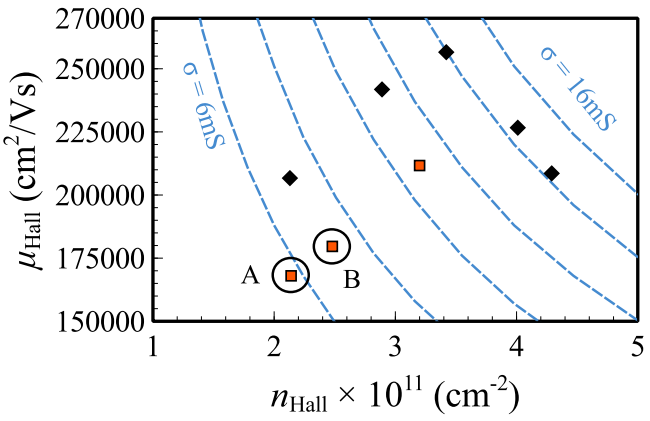

Figure 2. Measured Hall carrier mobility versus Hall sheet carrier density extracted from low temperature ($T < 5$ K) two-carrier analysis of Hall measurements up to $B = 0.5$ T. Data from two growth campaigns are shown (solid squares and solid diamonds). Samples A and B are indicated and broken lines display contours of constant sheet conductance.

lifetime, τ_q, from the slope, where the Dingle parameter, D_P, is given by:

$$D_P = \left(\frac{\Delta R_{xx}(B)}{R_0}\right)[4D_T(X_T)]^{-1}. \quad (4)$$

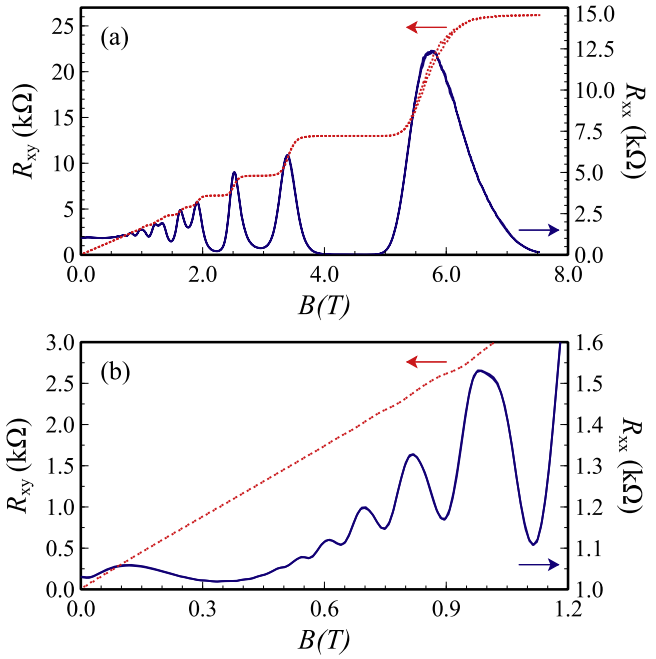

Figure 3. (a) The low temperature (2 K) longitudinal magnetoresistance (solid line), R_{xx}, and transverse magnetoresistance (dotted line), R_{xy} of an InSb 2DEG Hall bar device (sample A) up to high magnetic field ($B = 8.0$ T). (b) Magnified view of the SdH oscillations in the low field region ($B < 1.2$ T).

Typically, measurements of electron quantum lifetimes in GaAs 2DEG structures have been made at liquid helium temperatures ($T \approx 4.2$ K), with the application of relatively high magnetic fields ($B \approx 1-2$ T), or at millikelvin temperatures with more moderate magnetic fields. However, the thermal damping ($D_T(X_T)$) of an InSb 2DEG is much lower over the low field region than a GaAs 2DEG at these temperatures, thus the extraction of quantum lifetimes at lower magnetic fields is possible ($B \approx 0.5$ T) in InSb without the need for millikelvin temperatures.

The longitudinal magnetoresistance (R_{xx}) and transverse magnetoresistance (R_{xy}) of two samples, A and B were studied. Measurements were made at $T = 2$ K up to $B = 7.5$ T (sample A) and $T = 12$ mK up to $B = 8.0$ T (sample B) using a superconducting solenoid and the results for sample A are shown in figure 3(a). Well-defined Landau levels and quantum Hall plateaux are observed demonstrating a good quality 2DEG despite some apparent surface roughness/structure in Normaski phase contrast imaging. It is worth noting that the large Landé g-factor in InSb gives rise to spin separated Landau levels that diverge rapidly with magnetic field (Zeeman effect). Figure 3(b) shows the low field region ($B < 1.2$ T) where the Zeeman spin-splitting is not quite resolved, but clear SdH oscillations are observed down to $B \approx 0.5$ T. At the lowest magnetic fields, before the onset of SdH oscillations, the slowly varying magnetoresistance has previously been observed and attributed to electron–electron interactions [22], or sample inhomogeneity [23, 24], either of which are possible for the sample reported here. Other observations of a slowly varying background after the onset of SdH oscillations attributed the behaviour to inter-subband

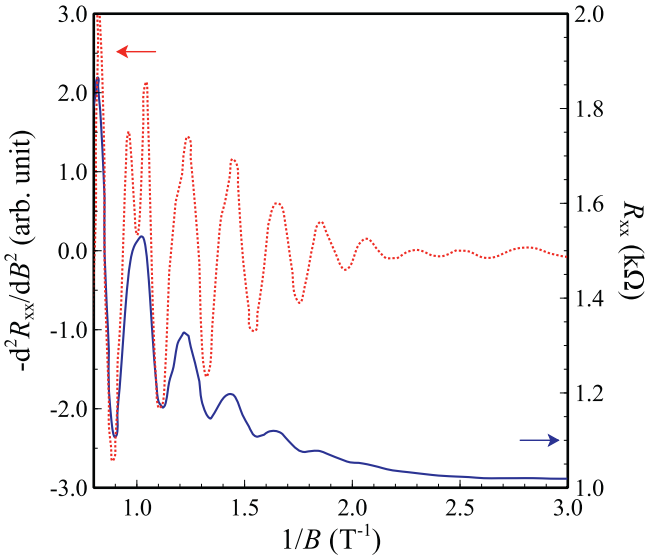

Figure 4. The low magnetic field longitudinal magnetoresistance (solid line), R_{xx}, against the inverse of the applied magnetic field for sample A. The negative double differential, $-d^2R_{xx}/dB^2$ of the longitudinal magnetoresistance (dotted line) is also plotted against $1/B$.

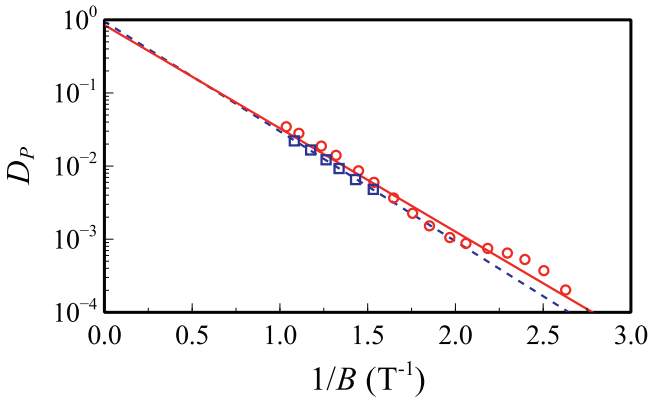

Figure 5. A semi-log 'Dingle' plot of the calculated Dingle parameter, D_p, for sample A (open circles) and Sample B (open squares) against the inverse of the applied magnetic field. Exponential fits to the data are also shown (sample A—solid line, sample B—dashed line), which yield calculated quantum lifetimes of $\tau_q \approx 0.107$ ps and $\tau_q \approx 0.103$ ps respectively.

scattering [25, 26]. However, as will be discussed in section 4, calculation of the subband energies in the InSb QW show that for sample A the Fermi level to second subband energy spacing is approximately two orders of magnitude greater than k_BT at 2 K. This means a similar attribution of inter-subband scattering for this observed effect is unlikely.

Plots of R_{xx} against $1/B$ are shown in figure 4, which demonstrates that the SdH oscillations observed are periodic in $1/B$ as expected [21]. The negative double differential ($-d^2R_{xx}/dB^2$), which is used to emphasise the SdH oscillations, is also shown in figure 4 and it can be seen that the periodic SdH oscillations are still discernible at $1/B \approx 2.5$ T^{-1} ($B \approx 0.4$ T). A Fourier transform of $-d^2R_{xx}/dB^2$ against $1/B$ taken over the input range $1/B = 1.30$ to $7.69\,T^{-1}$ (i.e. $B = 0.13$–0.77 T), results in a single oscillation corresponding to a fundamental field of $B_f = 4.40$ T (i.e. period $1/B_f \approx 0.227\,T^{-1}$). Since low magnetic field data is used to extract the fundamental oscillation period (before the onset of Zeeman spin-split Landau level observation), the fundamental field can be used to find the 2DEG carrier concentration, $n_s = 2.13 \times 10^{11}\,cm^{-2}$ where $n_s = 2eB_f/h$. This is in excellent agreement with the two-carrier Hall analysis ($n_{Hall} = 2.14 \times 10^{11}\,cm^{-2}$). There is also good agreement between the two-carrier Hall analysis and fundamental field extraction of the 2DEG carrier concentration for samples B and C with measured values of $n_{Hall} = 2.47 \times 10^{11}\,cm^{-2}$ and $2.90 \times 10^{11}\,cm^{-2}$ compared to $n_s = 2.54 \times 10^{11}\,cm^{-2}$ and $3.11 \times 10^{11}\,cm^{-2}$ respectively.

Dingle plots using magnetic field data below $B < 1$ T are shown in figure 5 for samples A and B. These plots use a modified zero resistance term, R_0, in equation (1) which accounts for the slowly varying background resistance. Exponential fits to the envelope data result in quantum lifetime of $\tau_q \approx 0.107$ ps and $\tau_q \approx 0.103$ ps for samples A and B respectively. The oscillation of the data points about the best fit line seen for sample A in figure 5 has previously been reported in GaAs and attributed to inter-subband scattering [27]. However, as noted earlier, the separation of the second subband and the Fermi level in our structure at $T = 2$ K is approximately ninety times greater than the thermal energy ($k_BT \approx 0.17$ meV). The origin of this oscillation is therefore unclear. In this analysis the best fit line intercept is expected to be unity and the freely fitted regression plots in figure 5 have intercepts of 0.85 and 0.95 for samples A and B respectively, which give high confidence in the validity of the fits. Syed *et al* [28] showed that 2DEG inhomogeneity can result in weaker SdH oscillations which yield an apparent τ_q value lower than the real value. Although this effect is expected to be small in our samples, which have an order of magnitude lower carrier density than in [28], we note that the τ_t/τ_q ratio we extract should therefore be considered an upper value.

A comparison of the transport lifetimes to the quantum lifetimes of the carriers in samples A and B result in transport lifetimes which are approximately 17 and 20 times longer than the quantum lifetimes respectively. These ratios are comparable with other materials systems such as InGaAs and GaAs, where τ_t/τ_q ratios ranging from 5 to 20 have been extracted experimentally [20, 21]. However, the ratios are much lower than would be expected if the dominant scattering mechanism arises from the remote ionized donors in the δ-doping layer. Using the analysis of Das Sarma and Stern [29] for screened ionized impurity scattering in a 2DEG, we predict a value $\tau_t/\tau_q > 100$ from remote ionized impurity scattering alone. Coleridge [20] accounted for a similar reduced τ_t/τ_q value in GaAs 2DEGs by additional scattering from ionized background impurities. In the next section we consider the effect of increasing this unintentional doping from background acceptors.

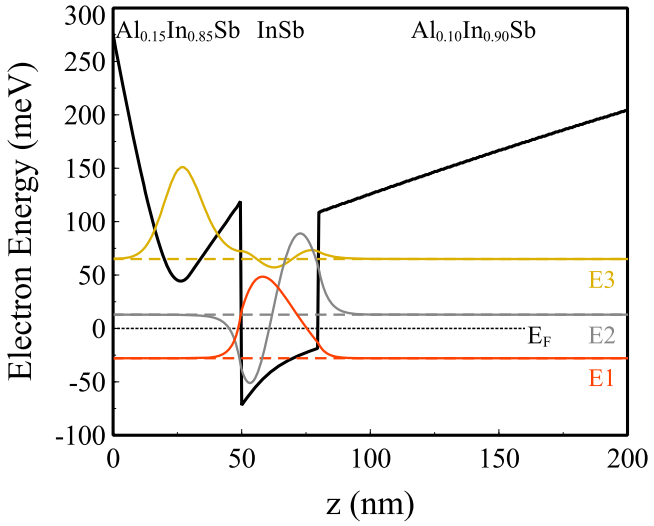

Figure 6. Calculated conduction band potential (thick solid line) in the top 200 nm at $T = 10$ K for a QW sheet density $n_{QW} \approx 2.2 \times 10^{11}$ cm^{-2}. The δ-doped layer is modelled with an exponential profile and a background acceptor density $N_{bkg} = 1 \times 10^{15}$ cm^{-3} is used. The three lowest energy solutions (dashed lines E1–E3) and their associated wavefunctions are shown. The Fermi level is at 0 meV (dotted line).

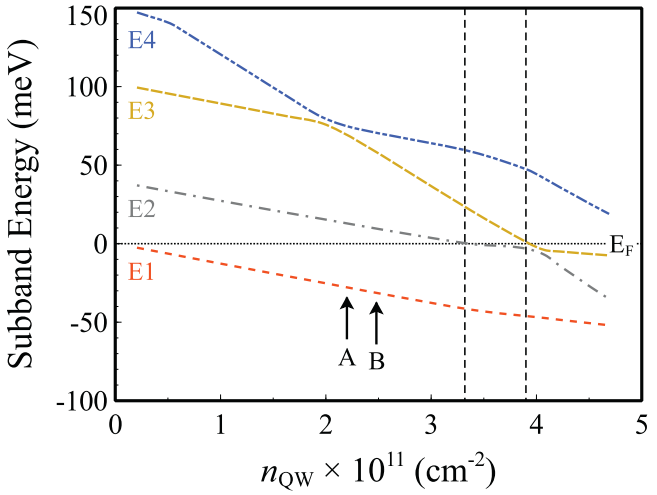

Figure 7. Calculated variation of the four lowest subband energy solutions (lines labelled E1–E4) as a function of QW electron density. The quantum well electron density for samples A and B are shown (arrows). The Fermi level is at 0 meV. The vertical dashed lines indicate where the subband filling changes.

4. Self-consistent Schrödinger–Poisson modelling

In order to understand the effect of varying the δ-doping concentration on the QW energy levels and 2DEG density (n_{QW}), the conduction and valence bands of the heterostructure described were modelled with a one-dimensional self-consistent Schrödinger–Poisson solver [30]. For brevity, a single temperature of $T = 10$ K was considered with input parameters taken after [19, 31, 32]. The background doping level was assumed to be low and p-type ($N_{bkg} = 1 \times 10^{15}$ cm^{-3}) and subsequent measurements on diagnostic structures grown in the same MBE reactor comprising only the 3 μm bottom $Al_{0.1}In_{0.9}Sb$ barrier exhibited a p-type carrier concentration below 5×10^{14} cm^{-3} at $T = 77$ K after taking into account surface depletion. Whilst difficult to assess with precision, flat layer growth indicates very low n-type background, with mobility that is reasonably comparable to pure bulk samples. Thus, it is highly unlikely that the measured p-type background for our alloy only layer includes a high level of compensation. However, to provide an upper limit from background impurity scattering, we have used an impurity concentration value in transport modelling (Section 5) that is, as a minimum, a factor of two greater than the measured p-type background. The Te δ-doping was modelled both as a simple 10 nm slab and with an exponential decrease from its nominal position towards the top surface [4]. Whilst the exponential decrease is a more realistic dopant profile, modelling of the δ-doping as a 10 nm slab provides a worst case (maximum) for the remote ionised impurity scattering rate (considered in section 5). The conduction band edge in the top 200 nm is shown in figure 6 for a Te doping density which results in a QW 2DEG density of $n_{QW} \approx 2.2 \times 10^{11}$ cm^{-2}. The Fermi level is at 0 meV. The three lowest electron energy levels are indicated by the dashed lines (denoted E1–E3), and their associated electron wavefunctions by solid lines. Higher subbands are omitted for clarity since none are occupied at $T = 10$ K in the doping range under consideration, where $n_{QW} < 4.6 \times 10^{11}$ cm^{-2}. Note that the E1 and E2 wavefunctions are localised subbands of the QW, whilst the E3 wavefunction is more localised around the δ-doping in the harmonic oscillator-like potential and only the E1 state is occupied at this doping density.

In figure 7, the variation of the four lowest energy solutions (E1–E4) are plotted as a function of QW electron density. It can be seen that there is an E3/E4 anti-crossing at $n_{QW} \approx 2 \times 10^{11}$ cm^{-2}, and an E2/E3 anti-crossing at $n_{QW} \approx 4 \times 10^{11}$ cm^{-2}. The electron state that is changing energy most rapidly with respect to the QW electron density is associated with the δ-doping induced potential well in the top barrier (i.e., E4 when $n_{QW} \leqslant 2 \times 10^{11}$ cm^{-2}, E3 when $n_{QW} = 2{-}4 \times 10^{11}$ cm^{-2}, and E2 when $n_{QW} \geqslant 2 \times 10^{11}$ cm^{-2}).

In figure 7, at the value $n_{QW} \approx 2.2 \times 10^{11}$ cm^{-2} it can be seen that the second (E2) subband is 15 meV above the Fermi level and is therefore empty at $T = 2$ K (sample A). With increasing occupancy of the 2DEG up to $n_{QW} \approx 2.5 \times 10^{11}$ cm^{-2} the energy difference between the Fermi level and the second subband (E2) decreases, but remains much greater than $k_B T$ at $T = 12$ mK (sample B).

The dashed lines in figure 7 indicate where the next highest subband starts to fill. That is, in the leftmost region only the E1 state is filling, in the centre region both the E1 and E2 states are filling, and in the rightmost region all three states E1–E3 are filling. Note the filling rate is faster for the state associated with the doping in the top barrier. Indeed, beyond $n_{QW} \approx 4.0 \times 10^{11}$ cm^{-2}, further increase in Te δ-

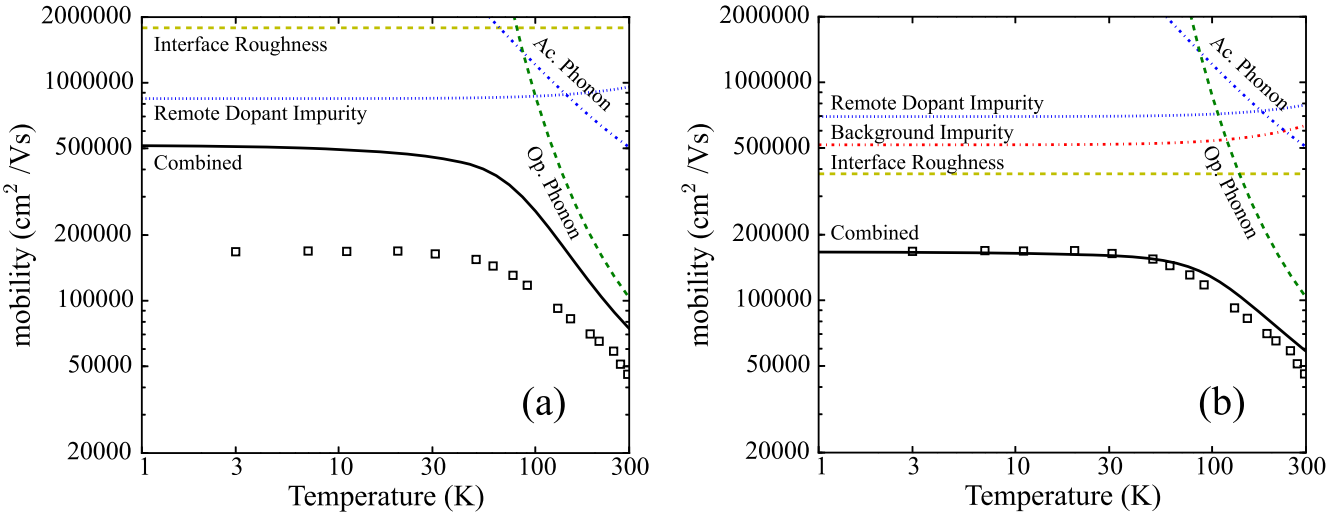

Figure 8. Calculated mobility variation with temperature at $n_{QW} = 2.2 \times 10^{11}\,cm^{-2}$ and 20 nm interface roughness lateral parameter (Λ) for two different background acceptor concentrations and interface roughness, Δ. (a) $N_{bkg} = 1 \times 10^{15}\,cm^{-3}$ with $\Delta = 3$ ml, and; (b) $N_{bkg} = 1 \times 10^{16}\ cm^{-3}$ with $\Delta = 6.5$ ml. The various scattering mechanisms in the model are labelled and measured data from sample A shown (open squares).

doping does not increase n_{QW} proportionately as most of the extra electrons stay in the top barrier.

5. Transport mobility modelling

The low transport to quantum lifetime ratio has been investigated further by modelling the transport mobility in a manner consistent with the Schrödinger–Poisson modelling. In particular, the δ-doping, QW 2DEG density and background doping concentration are interdependent, so the Te dopant level required for a given n_{QW} and N_{bkg} must be found iteratively. Our mobility model considers several physical parameters, namely the Te dopant profile in the top barrier, the unintentional background doping and the QW interface roughness. Details of the calculation of individual scattering components can be found elsewhere [4, 33, 34]. Scattering times for scattering by remote ionized impurities, background ionized impurities, interface roughness, acoustic phonons and optic phonons were calculated and combined using Matthieson's rule. Our model assumes infinite QW barriers and an ideal δ-doping plane, which dominates the carrier quantum lifetime, rather than a more realistic exponential decay away from its nominal position. This assumption results in a worst case scenario for the remote ionised impurity scattering rate and hence the shortest scattering times, thus a lower transport-to-quantum lifetime ratio. The transport mobility and τ_t/τ_q values we present are therefore worst case (lowest) values. At the low QW carrier densities examined here intersubband scattering or electron–electron scattering is not considered, and alloy scattering in the barriers is neglected.

Figures 8(a) and (b) show the calculated combined mobility against temperature at a QW electron density of $n_{QW} = 2.2 \times 10^{11}\,cm^{-2}$, with different scattering component strengths. The transport model material parameters were taken from [33, 35] with a temperature dependent calculated effective mass from a four band **k.p** model with $m^* = 0.0195\,m_e$ at 10 K. The resultant mobility from each different scattering process is also shown, emphasising the relative influence of each mechanism. The predominant scattering process at low temperature arises from remote ionized donor impurities and from phonon scattering at room temperature.

In figure 8(a) the background acceptor concentration, $N_{bkg} = 1 \times 10^{15}\,cm^{-2}$ and the interface roughness, $\Delta = 3$ ml over a lateral parameter $\Lambda = 20$ nm, yielding modelled values of $\mu = 515\,000\,cm^2\,V^{-1}\,s^{-1}$ and $\tau_t/\tau_q = 157$ at $T = 10$ K. The modelled mobility and τ_t/τ_q ratio are considerably larger than the measured values.

In order to reduce the modelled mobility and τ_t/τ_q ratio to the measured values, we must increase either the level of background doping and/or increase the interface roughness. A consequence of increasing background acceptor doping is a necessary compensating increase in the remote Te doping level in order to maintain a given QW 2DEG density. Thus, the conduction band profile is changed, most noticeably in the upper barrier around the δ-doping region. For example, at $T = 10$ K the Schrödinger–Poisson modelling shows that for values of $N_{bkg} \geqslant 4 \times 10^{15}\,cm^{-3}$, the position of the E2 and E3 wavefunctions are reversed. This means that when E2 starts filling, at peak mobility, the associated E2 wavefunction is localised predominantly in the upper barrier where alloy scattering can significantly reduce the in plane mobility. Whilst the increased N_{bkg} value can account for the peak mobility occurring at $n_{QW} = 3.1 \times 10^{11}\,cm^{-2}$, the calculated mobility is still too high. We find that N_{bkg} must be increased further to obtain a good fit, within the constraint $N_{bkg} < 1.5 \times 10^{16}\,cm^{-2}$. We find that higher values of N_{bkg} are incompatible with the Schrödinger–Poisson solution which predicts a second subband located around the Te δ-dopant starts to populate before the QW reaches the required electron density ($n_{QW} = 2.2 \times 10^{11}\,cm^{-2}$).

In figure 8(b) the background acceptor concentration is raised to $N_{bkg} = 1 \times 10^{16}$ cm^{-2}, and the increased scattering reduces the modelled values to $\mu = 170\,000$ cm^2 V^{-1} s^{-1} and $\tau_t/\tau_q = 54$ at $T = 10$ K. Although the modelled transport mobility is now very close to the measured value, the τ_t/τ_q ratio is still too large.

We can approach the measured τ_t/τ_q ratio in our model by increasing the interface roughness asperity parameter (Δ) and reducing the interface roughness lateral parameter (Λ), however the input parameter values required in our model to fit the measured mobility, namely $N_{bkg} = 1 \times 10^{16}$ cm^{-3} and $\Delta = 6.5$ ml, are already higher than expected when considering the measured value of background acceptors, $N_{bkg} < 5 \times 10^{14}$ cm^{-3} and such QW width fluctuations have not been previously observed in high resolution transmission electron microscope images of the InSb QW. To achieve a τ_t/τ_q ratio close to the measured value of 17 from sample A requires an interface roughness asperity parameter of $\Delta = 8$ ml or greater with a lateral roughness of $\Lambda = 10$ nm, which is unrealistically large and furthermore does not at the same time predict the measured mobility. In order to explain the Hall measurements we infer there must be at least one other scattering mechanism and further investigation is required to identify realistic additional scattering mechanisms.

6. Conclusion

We have made magnetotransport measurements on a series of InSb/AlInSb QW 2DEGs with different carrier densities. A Schrödinger–Poisson model has been used to correlate band filling with definite regimes observed in mobility verses carrier density. Due to the low effective mass of InSb, the electron quantum lifetime of carriers in InSb/In$_x$Al$_{1-x}$Sb QW structures can be extracted from magnetotransport measurements at very low magnetic field ($B < 0.8$ T) without the need for millikelvin sample temperatures. The SdH oscillations observed in the longitudinal magnetoresistance are associated with the QW 2DEG and are still discernible at fields as low as $B = 0.4$ T despite modest mobility extracted from Hall analysis. The extracted ratio of transport to quantum lifetimes, $\tau_t/\tau_q \approx 17$ and $\tau_t/\tau_q \approx 20$ are similar to values reported in other binary QW 2DEG systems, but are inconsistent with predictions from a transport model which assumes that remote ionized donors are the dominant scattering mechanism. At a carrier density $n_{QW} = 2.2 \times 10^{11}$ cm^{-2}, where only one QW subband is occupied, we find the low τ_t/τ_q ratio and low electron transport mobility cannot be simultaneously explained by reasonable levels of background impurities or well width fluctuations. Thus, there is at least one additional unaccounted for scattering mechanism, most likely arising from structural defects.

Acknowledgments

The authors would like to thank Dr Richard Jefferies at the University of Warwick, School of Engineering for assistance with background doping measurement. The authors acknowledge funding for this work from the UK Engineering and Physical Sciences Research Council grant EP/L012995/1. Data supporting this research is openly available from the Cardiff University Research Portal at http://doi.org/10.17035/d.2016.0008719302.

ORCID

D G Hayes https://orcid.org/0000-0002-2303-1622
C P Allford https://orcid.org/0000-0002-3798-9014
G V Smith https://orcid.org/ 0000-0003-1069-5347
C McIndo https://orcid.org/0000-0003-2253-7012

References

[1] Madelung O, Rössler U and Schulz M 2002 *Landolt and Bornstein—Group IV Elements,(IV–IV) and (III–V) Compounds. Part b—Electronic, Transport, Optical and Other Properties* (Berlin: Springer)
[2] Yi W *et al* 2015 Gate-tunable high mobility remote-doped InSb/In$_{1-x}$Al$_x$Sb quantum well heterostructures *Appl. Phys. Lett.* **106** 142103
[3] Pooley O J, Gilbertson A M, Buckle P D, Hall R S, Emeny M T, Fearn M, Halsall M P, Cohen L F and Ashley T 2010 Quantum well mobility and the effect of gate dielectrics in remote doped InSb/Al$_x$In$_{1-x}$ Sb heterostructures *Semicond. Sci. Technol.* **25** 125005
[4] Orr J M S, Gilbertson A M, Fearn M, Croad O W, Storey C J, Buckle L, Emeny M T, Buckle P D and Ashley T 2008 Electronic transport in modulation-doped InSb quantum well heterostructures *Phys. Rev.* B **77** 165334
[5] Mourik V *et al* 2012 Signatures of Majorana fermions in hybrid superconductor-semiconductor nanowire devices *Science* **336** 1003–7
[6] Deng M T, Yu C L, Huang G Y, Larsson M, Caroff P and Xu H Q 2012 Anomalous zero-bias conductance peak in a Nb–InSb Nanowire–Nb hybrid device *Nano Lett.* **12** 6414–9
[7] Nedniyom B, Nicholas R J, Emeny M T, Buckle L, Gilbertson A M, Buckle P D and Ashley T 2009 Giant enhanced g-factors in an InSb two-dimensional gas *Phys. Rev.* B **80** 125328
[8] Qu F *et al* 2016 Quantized conductance and large g-factor anisotropy in InSb quantum point contacts *Nano Lett.* **16** 7509–13
[9] van den Berg J W G, Nadj-Perge S, Pribiag V S, Plissard S R, EPAM B, Frolov S M and Kouwenhoven L P 2013 Fast spin–orbit qubit in an indium antimonide nanowire *Phys. Rev. Lett.* **110** 66806
[10] Li R, You J Q, Sun C P and Nori F 2013 Controlling a nanowire spin–orbit qubit via electric-dipole spin resonance *Phys. Rev. Lett.* **111** 86805
[11] Awschalom D D, Bassett L C, Dzurak A S, Hu E L and Petta J 2013 Quantum spintronics: engineering and manipulating atom-like spins in semiconductors *Science* **339** 1174–9
[12] Umansky V, Heiblum M, Levinson Y, Smet J, Nübler J and Dolev M 2009 MBE growth of ultra-low disorder 2DEG with mobility exceeding 35 $\times$ 10^{6}cm^2/Vs *J. Cryst. Growth* **311** 1658–61
[13] Harris J J *et al* 2001 Relationship between classical and quantum lifetimes in AlGaN/GaN heterostructures *Semicond. Sci. Technol.* **16** 402–5

[14] Çelik H, Cankurtaran M, Bayrakli A, Tiras E and Balkan N 1997 Well-width dependence of the in-plane effective mass and quantum lifetime of electrons in multiple quantum wells *Semicond. Sci. Technol.* **12** 389–95
[15] Coleridge P, Stoner R and Fletcher R 1989 Low-field transport coefficients in GaAs/$Ga_{1-x}Al_xAs$ heterostructures *Phys. Rev.* B **39** 1120–4
[16] Gilbertson A M, Buckle P D, Emeny M T, Ashley T and Cohen L F 2011 Suppression of the parasitic buffer layer conductance in InSb/$Al_xIn_{1-x}Sb$ heterostructures using a wide-band-gap barrier layer heterostructures *Phys. Rev.* B **84** 75474
[17] Pooley O J, Gilbertson A M, Buckle P D, Hall R S, Buckle L, Emeny M T, Fearn M, Cohen L F and Ashley T 2010 Transport effects in remote-doped InSb/$Al_xIn_{1-x}Sb$ heterostructures *New J. Phys.* **12** 53022
[18] Reed M, Kirk W and Kobiela P 1986 Investigation of parallel conduction in GaAs/$Al_xGa_{1-x}As$ modulation-doped structures in the quantum limit *IEEE J. Quantum Electron.* **22** 1753–9
[19] Dai N, Brown F, Doezema R E, Chung S J, Goldammer K J and Santos M B 1998 Determination of the concentration and temperature dependence of the fundamental energy gap in $Al_xIn_{1-x}Sb$ *Appl. Phys. Lett.* **73** 3132–4
[20] Coleridge P T 1991 Small-angle scattering in two-dimensional electron gases *Phys. Rev.* B **44** 3793–801
[21] Coleridge P T, Zawadzki P and Sachrajda A S 1994 Peak values of resistivity in high-mobility quantum-Hall-effect samples *Phys. Rev.* B **49** 10798–801
[22] Lee P A and Ramakrishnan T V 1985 Disordered electronic systems *Rev. Mod. Phys.* **57** 287–337
[23] Schneider W, Bruhns H and Hübner K 1980 Interaction of transverse magnetoresistance effects in extrinsic and intrinsic InSb *J. Phys. Chem. Solids* **41** 313–21
[24] Branford W R, Husmann A, Solin S A, Clowes S K, Zhang T, Bugoslavsky Y V and Cohen L F 2005 Geometric manipulation of the high-field linear magnetoresistance in InSb epilayers on GaAs (001) *Appl. Phys. Lett.* **86** 202116
[25] Sander T H, Holmes S N, Harris J J, Maude D K and Portal J C 1998 Determination of the phase of magneto-intersubband scattering oscillations in heterojunctions and quantum wells *Phys. Rev.* B **58** 13856–62
[26] Raikh M E and Shahbazyan T V 1994 Magnetointersubband oscillations of conductivity in a two-dimensional electronic system *Phys. Rev.* B **49** 5531–40
[27] Coleridge P T 1990 Inter-subband scattering in a 2D electron gas *Semicond. Sci. Technol.* **5** 961–6
[28] Syed S, Manfra M J, Wang Y J, Molnar R J and Stormer H L 2004 Electron scattering in AlGaN/GaN structures *Appl. Phys. Lett.* **84** 1507–9
[29] Das Sarma S and Stern F 1985 Single-particle relaxation time versus scattering time in an impure electron gas *Phys. Rev.* B **32** 8442–4
[30] Tan I-H, Snider G L, Chang L D and Hu E L 1990 A self-consistent solution of Schrödinger–Poisson equations using a nonuniform mesh *J. Appl. Phys.* **68** 4071
[31] Apel J R, Poehler T O, Westgate C R and Joseph R I 1971 Study of the shape of cyclotron-resonance lines in indium antimonide using a far-infrared laser *Phys. Rev.* B **4** 436–51
[32] Elkenany E B 2015 Theoretical investigations of electronic, optical and mechanical properties for GaSb and AlSb semiconductors under the influence of temperature *Spectrochim. Acta* A **150** 15–20
[33] Shao Y, Solin S A, Ram-Mohan L R and Yoo K-H 2007 Optimizing the physical contribution to the sensitivity and signal to noise ratio of extraordinary magnetoresistance quantum well structures *J. Appl. Phys.* **101** 123704
[34] Davies J H 1998 *The Physics of Low-Dimensional Semiconductors: An Introduction* (Cambridge: Cambridge University Press) pp 356–65
[35] Adachi S 2005 *Properties of Group-IV, III-V and II-VI Semiconductors* (New York: Wiley) pp 173–93